

## Symmetrization of Thin Freestanding Liquid Films via a Capillary-Driven Flow

Vincent Bertin,<sup>1,2,†</sup> John Niven,<sup>3,†</sup> Howard A. Stone,<sup>4</sup> Thomas Salez<sup>1,5</sup>,, Elie Raphaël<sup>2</sup>,, and Kari Dalnoki-Veress<sup>2,3,\*</sup>

<sup>1</sup>Univ. Bordeaux, CNRS, LOMA, UMR 5798, 33405 Talence, France

<sup>2</sup>UMR CNRS Gulliver 7083, ESPCI Paris, PSL Research University, 75005 Paris, France

<sup>3</sup>Department of Physics and Astronomy, McMaster University, Hamilton, Ontario L8S 4M1, Canada

<sup>4</sup>Department of Mechanical and Aerospace Engineering, Princeton University, Princeton, New Jersey 08544, USA

<sup>5</sup>Global Station for Soft Matter, Global Institution for Collaborative Research and Education, Hokkaido University, Sapporo, Hokkaido 060-0808, Japan



(Received 16 December 2019; revised manuscript received 2 March 2020; accepted 21 April 2020; published 8 May 2020)

We present experiments to study the relaxation of a nanoscale cylindrical perturbation at one of the two interfaces of a thin viscous freestanding polymeric film. Driven by capillarity, the film flows and evolves toward equilibrium by first symmetrizing the perturbation between the two interfaces and eventually broadening the perturbation. A full-Stokes hydrodynamic model is presented, which accounts for both the vertical and lateral flows and which highlights the symmetry in the system. The symmetrization time is found to depend on the membrane thickness, surface tension, and viscosity.

DOI: [10.1103/PhysRevLett.124.184502](https://doi.org/10.1103/PhysRevLett.124.184502)

Surface tension will smoothen interfacial perturbations on a thin liquid film, since the curvature of the perturbation profile induces a Laplace pressure that drives flow. This capillary-driven leveling causes the brush strokes on paint to flatten, or the spray of small droplets to form a uniform film. Such flows have been studied in detail and much of the framework is provided by the lubrication theory (a simplified version of the Navier-Stokes equations appropriate for laminar thin-film flow), where one can assume that flow in the plane of the film dominates and that the velocity vanishes at the solid-liquid interface [1,2]. Freestanding liquid films do not support a shear-stress at *both* liquid-air interfaces, which modifies the boundary conditions and results in a different phenomenology [1]. These boundary conditions arise in biological membranes [3], soap films [4–9], liquid-crystal films [10–12], fragmentation processes [13], or energy-harvesting technologies [14].

The dynamics of liquid sheets has been studied extensively [15,16] and shows similarities with the mechanics of elastic plates. The evolution can be described with two dominant modes, which are the stretching and bending modes associated with linear momentum and torque balances. At macroscopic scales, a viscous sheet experiences bending instabilities such as wrinkling [17–20] and folding [21] when submitted to compression. Such viscous buckling phenomena occur in tectonic-plate dynamics [22,23] and industrial float-glass processes [24–27].

In thin freestanding films, surface tension is dominant and stabilizes the interfaces against buckling [15]. Most theoretical models in this context assume that the interfaces are mirror symmetric and thus focus on the stretching mode, also called the symmetric mode. This approach is

employed to study the rupture dynamics of films in the presence of disjoining forces that destabilize long waves in thin films [28–35]. Using nanometric freestanding polystyrene (PS) films, Ilton *et al.* observed that a film with initially asymmetric interfaces symmetrized over short timescales [36]. This symmetrization was attributed to flow perpendicular to the film, but the dynamics was not accessible experimentally.

Here we study the viscocapillary relaxation of a nanoscale cylindrical perturbation initially present at one interface of a thin freestanding PS film. Both the symmetric (viscous stretching) and antisymmetric (viscous bending) modes are probed with experiments (Fig. 1). Atomic force microscopy (AFM) is used to obtain the profiles of the top and bottom interfaces [Fig. 1(a)]. A full-Stokes flow linear hydrodynamic model is developed to characterize the dynamics of the two modes. To provide intuition for the energy dissipation, we turn to the schematic excess surface energy as a function of time, shown in Fig. 1(d). Initially, the top interfacial profile, denoted  $h_+$ , has a high excess energy due to the additional interface that forms the perturbation, while the bottom interfacial profile  $h_-$  is flat and has no excess surface energy. The excess energy resulting from the perturbation drives flow that is mediated by viscosity  $\eta$ . As the film evolves, the total energy dissipates as the excess interface decreases. With decreasing global energy, the symmetrization process requires energy transfer from the top interface to the bottom, dominated by vertical flow. Once both interfaces are symmetric, they relax in tandem, dominated by lateral flow. Remarkably, the temporal evolution of the interfacial profiles, when appropriately decomposed into their symmetric and antisymmetric components, obey power laws.

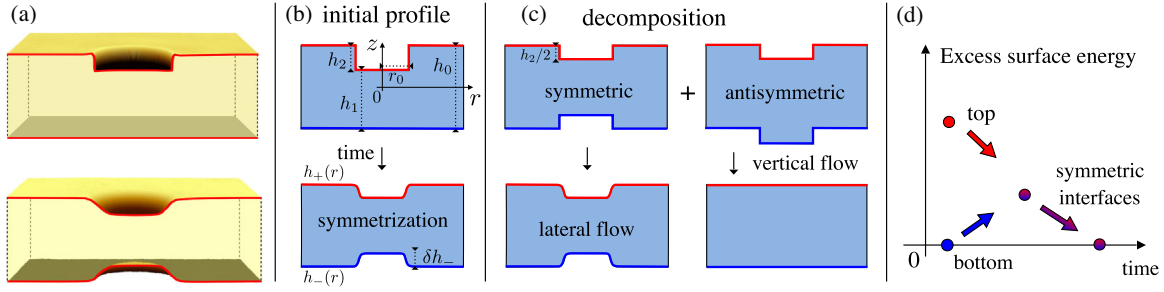


FIG. 1. (a) AFM images of sample with surface perturbation with initial radius  $r_0 \approx 6.2 \mu\text{m}$  and depth  $h_2 \approx 80 \text{ nm}$  (top) and after 500 min of annealing (bottom). (b) Schematic of an initial cylindrical hole of depth  $h_2$  and radius  $r_0$ , on one side of a polystyrene freestanding film, which evolves toward symmetric. (c) Symmetric-asymmetric decomposition of the interfacial profiles. A symmetric profile leads to lateral flow, while an antisymmetric one leads to vertical flow. (d) Schematic of the evolution of the excess surface energy. The top and bottom surface energies equalize before vanishing in tandem on larger timescales.

We construct freestanding films with a nanometric perturbation by stacking a film with small cylindrical pores on a second thicker film that is intact, following a method similar to that previously described [36,37]. This process results in a film with a cylindrical hole at one interface. PS with molecular weight  $M_w = 183 \text{ kg/mol}$  (Polymer Source, polydispersity index = 1.06) is dissolved in toluene (Fisher Scientific, Optima) with concentrations of 2% and 7.5% by weight. Films are prepared by spin coating from solution onto freshly cleaved mica (Ted Pella) and annealed at  $130^\circ\text{C}$  in vacuum ( $1 \times 10^{-5} \text{ mbar}$ ) for 24 h. The films have thicknesses  $h_1 = 530$  and  $h_2 = 80 \text{ nm}$ , as measured using ellipsometry (Accurion, EP3). The freestanding films are prepared in a two-step process inspired by Backholm *et al.* [37]. Films are floated from mica substrates onto the surface of ultrapure water ( $18.2 \text{ M}\Omega \text{ cm}$ ) and picked up on a thin circular steel washer (thickness = 0.1 mm, AccuGroup), creating a freestanding film supported only at the edges of the washer. The thicker film, with  $h_1 = 530 \text{ nm}$ , is picked up on a washer with an internal diameter of 3 mm and briefly heated above the glass-transition temperature  $T_g \approx 100^\circ\text{C}$  on a hot stage (Linkam, UK), resulting in a smooth, taugt film. Similarly, the thinner film with  $h_2 = 80 \text{ nm}$  is transferred from the water to a washer with an internal diameter of 5 mm. This film is heated ( $100^\circ\text{C}/\text{min}$ ) to  $125^\circ\text{C}$  under a microscope for several seconds and holes are nucleated on small defects in the film, which grow with time [34,38–40]. When the holes become visible, the film is quenched to room temperature, resulting in a freestanding film with randomly distributed holes of diameter 1–10  $\mu\text{m}$ . The two films are then placed in contact and adhere through van der Waals forces, and the larger diameter washer can be removed. This process results in a freestanding film of thickness  $h_0 = h_1 + h_2$ , with cylindrical holes of depth  $h_2$  [Figs. 1(a) and (b)].

The films are annealed on the hot stage at  $T = 130^\circ\text{C}$  and covered with a coverslip to ensure a uniform temperature with  $\eta \approx 1.1 \times 10^8 \text{ Pa s}$  and surface tension  $\gamma \approx 30 \text{ mJ/m}^2$  [41]. After some annealing time, the film is

quenched to room temperature, thus returning to the glassy state where flow becomes arrested. The surface profiles of three holes in the same film are then measured after each annealing step using AFM (Bruker, Multimode). Since the film is freestanding and has two polymer-air interfaces, both the top and bottom profiles are measured. The angular-averaged profiles are extracted at each time and provide a cross section of the film as it evolves (Fig. 2).

Initially, the film has different curvature gradients at the top and bottom interfaces, resulting in pressure gradients in vertical and lateral directions. The initial response of the film in the vicinity of the hole is for the bottom interface to buckle downward, forming a small ( $\sim 10 \text{ nm}$ ) elastic bump. This feature is not a result of a viscoelastic response to interfacial forces [42], as this would generate an opposite displacement. We speculate that this feature is the result of residual stresses associated with sample preparation: it is known that during hole formation the shear-strain rate near the rim of the hole perturbs polymer chains from equilibrium [39,40]. Upon adhering the two films, the nonequilibrium chains in the rim can impart a tension along the rim

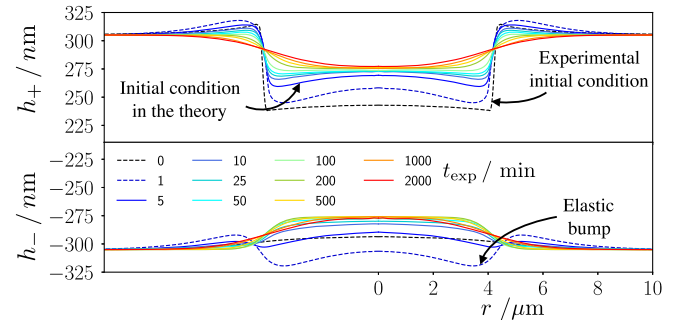


FIG. 2. AFM profiles of the top and bottom interfaces of a freestanding hole with  $h_2 = 80 \text{ nm}$ ,  $h_0 = 610 \text{ nm}$ , and  $r_0 = 4.2 \mu\text{m}$  (Fig. 1), at various annealing times  $t_{\text{exp}}$  as indicated. An “elastic bump” is seen at  $t_{\text{exp}} = 1 \text{ min}$  due to the residual stresses in the film from the sample preparation. The viscous model takes the profiles at 5 min as initial profiles, in order to ignore any prior elastic effect.

acting to compress and buckle the sample. As the film is annealed, the elastic bump relaxes on a timescale  $\sim 5$  min, which is similar to the macromolecular relaxation time for PS (the reptation time at  $T = 130^\circ\text{C}$  is  $\sim 13$  min [43]).

After relaxation of the bump, the flow depends on capillarity and viscosity. First, there is vertical flow to equilibrate the Laplace pressures and symmetrize the top and bottom interfaces. Indeed, two symmetric interfacial profiles are observed at times larger than  $\sim 200$  min. Subsequently, the symmetric interfaces evolve in tandem through lateral flow and dissipate the excess surface energy [30]. The film is annealed for  $\sim 2000$  min before rupturing.

We now turn to a theoretical description. The polymer is assumed to be a Newtonian fluid with viscosity  $\eta$ . We introduce cylindrical coordinates  $(r, z)$ , as well as the Hankel transforms [44] of the velocity field  $\vec{u}(r, z, t) = (u_r, u_z)$  and of the interfacial profiles  $h_\pm(r, t)$ :  $\tilde{u}_r(k, z, t) = \int_0^\infty dr r u_r(r, z, t) J_1(kr)$ ,  $\tilde{u}_z(k, z, t) = \int_0^\infty dr r u_z(r, z, t) J_0(kr)$ , and  $\tilde{h}_\pm(k, t) = \int_0^\infty dr r h_\pm(r, t) J_0(kr)$ , where  $t$  is time, and the  $J_i$  are the Bessel functions of the first kind with indices  $i = 0, 1$ . Injecting these into the steady Stokes equations, we find  $\partial_z^3 \tilde{u}_r + k \partial_z^2 \tilde{u}_z - k^2 \partial_z \tilde{u}_r - k^3 \tilde{u}_z = 0$  and  $\partial_z \tilde{u}_z + k \tilde{u}_r = 0$ , which gives

$$\begin{aligned} \tilde{u}_r &= -\frac{1}{k}(kA + kzC + D) \sinh(kz) \\ &\quad -\frac{1}{k}(kB + kzD + C) \cosh(kz), \end{aligned} \quad (1a)$$

$$\tilde{u}_z = (A + zC) \cosh(kz) + (B + zD) \sinh(kz), \quad (1b)$$

where  $A(t)$ ,  $B(t)$ ,  $C(t)$ , and  $D(t)$  are integration constants. The depth of the hole is assumed to be small in comparison with the thickness of the film, which is valid for the experiments, and we linearize the problem by writing the profiles as  $h_\pm = \pm h_0/2 + \delta h_\pm$ , where the perturbations  $\delta h_\pm$  are small compared to the film thickness  $h_0$ . We assume no-shear-stress boundary conditions at both fluid-air interfaces and neglect nonlinearities from the scalar projections of the normal and tangential vectors to the interface, which gives

$$\begin{aligned} &\left(\pm kA + C \frac{kh_0}{2}\right) \sinh\left(\frac{kh_0}{2}\right) \\ &+ \left(kB \pm D \frac{kh_0}{2}\right) \cosh\left(\frac{kh_0}{2}\right) = \pm \frac{\gamma k^2}{2\eta} \delta h_\pm, \end{aligned} \quad (2a)$$

$$\begin{aligned} &\left(kA \pm C \frac{kh_0}{2} + D\right) \cosh\left(\frac{kh_0}{2}\right) \\ &+ \left(\pm kB + D \frac{kh_0}{2} \pm C\right) \sinh\left(\frac{kh_0}{2}\right) = 0. \end{aligned} \quad (2b)$$

Finally, we invoke the linearized kinematic conditions  $\partial_t \tilde{h}_\pm = \tilde{u}_z(k, z = \pm h_0/2, t)$  and obtain a set of coupled linear differential equations. The symmetric-antisymmetric

decomposition, through  $\tilde{h}_{\text{sym}} = \delta \tilde{h}_+ - \delta \tilde{h}_-$  and  $\tilde{h}_{\text{anti}} = \delta \tilde{h}_+ + \delta \tilde{h}_-$  [see Fig. 1(c)], appears as the natural modal decomposition for this system. These two modes relax independently to equilibrium, with distinct decay rates  $\lambda_{\text{sym}}$  and  $\lambda_{\text{anti}}$ , since

$$\partial_t \tilde{h}_{\text{sym}} = -\frac{\gamma k}{\eta} \frac{\sinh^2(\frac{kh_0}{2})}{\sinh(kh_0) + kh_0} \tilde{h}_{\text{sym}} = -\lambda_{\text{sym}} \tilde{h}_{\text{sym}}, \quad (3a)$$

$$\partial_t \tilde{h}_{\text{anti}} = -\frac{\gamma k}{\eta} \frac{\cosh^2(\frac{kh_0}{2})}{\sinh(kh_0) - kh_0} \tilde{h}_{\text{anti}} = -\lambda_{\text{anti}} \tilde{h}_{\text{anti}}. \quad (3b)$$

The dimensionless decay rates are plotted in Fig. 3 as a function of the dimensionless wave number  $kh_0$ . For each rate, two asymptotic behaviors can be distinguished. At large  $kh_0$ , both rates exhibit the same asymptotic behavior:  $\lambda(k) \sim \gamma k/\eta$ . At small  $kh_0$ , the symmetric rate becomes identical to the one in the symmetric long-wave freestanding film model:  $\lambda_{\text{sym}} \sim \gamma h_0 k^2/(8\eta)$  [30,36], and thus Eq. (3) reduces to a heatlike equation in Hankel space, with a diffusion coefficient  $\gamma h_0/(8\eta)$ . In the same limit, the antisymmetric rate has a different scaling law:  $\lambda_{\text{anti}} \sim 6\gamma/(\eta h_0^3 k^2)$ . Therefore, long waves are quickly damped for the antisymmetric mode. We note that  $\lambda_{\text{anti}}$  has a minimum at  $k \simeq 3.28/h_0$ , corresponding to a slowest mode, which sets the relaxation dynamics.

The model assumes a Newtonian fluid and must be compared to experimental profiles corresponding to annealing times longer than the polymeric relaxation time. Thus, we take the experimental profiles at  $t_{\text{exp}} = 5$  min as the initial conditions for the model (Fig. 2). Equations (3a) and (3b) are solved, yielding

$$\tilde{h}_{\text{sym/anti}}(k, t) = \tilde{h}_{\text{sym/anti}}(k, 0) \exp[-\lambda_{\text{sym/anti}}(k)t], \quad (4)$$

where  $t = t_{\text{exp}} - 5$  min. The symmetric and antisymmetric modes are shown in Fig. 4 and reveal a qualitative

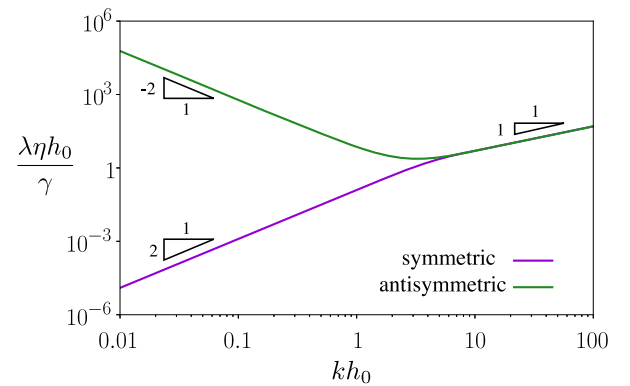


FIG. 3. Dimensionless decay rates of the symmetric and antisymmetric modes [Eqs. (3a) and (3b)] as a function of the dimensionless wave number. The slope triangles indicate power-law exponents.

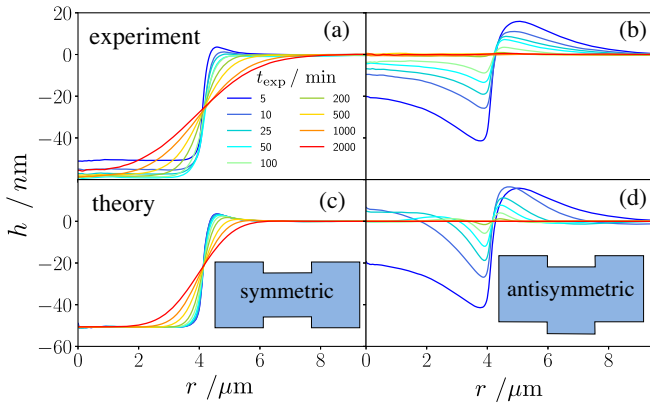


FIG. 4. (a) Symmetric and (b) antisymmetric modes of the experimental (angular-averaged) profiles for various times. The colors correspond to the same times as in Fig. 2. (c) Symmetric and (d) antisymmetric modes of the theoretical profiles, according to Eq. (4), for various times, and with the experimental profiles at  $t_{\text{exp}} = 5$  min as the initial conditions ( $t = 0$ ).

agreement between theory and experiment. Notably, the symmetric mode exhibits a self-similar behavior when plotted (not shown) as a function of the variable  $(r - r_0)/t^{1/2}$ . This result for freestanding films is to be compared to the capillary leveling of a cylindrical hole in a film supported on a substrate, which is self-similar in  $(r - r_0)/t^{1/4}$  [37]. In contrast, the antisymmetric mode vanishes, on a timescale on the order of  $\sim 200$  min, resulting in top and bottom interfacial profiles that are mirror symmetric, as observed in Fig. 2. The long waves are damped more quickly than the short ones, in agreement with the limiting scaling behaviors of  $\lambda_{\text{anti}}(k)$  (Fig. 3).

A measure of proximity to equilibrium lies in the excess capillary energy, which is proportional to the excess surface area  $S$  with respect to a flat film  $S_i = 2\pi \int_0^\infty dr r (\sqrt{1 + (\partial_r h_i)^2} - 1)$ , where  $i$  can refer to  $+$ ,  $-$ , sym, or anti, depending on the profile or mode in question. In the small-slope limit (valid at  $t_{\text{exp}} > 5$  min),  $S_i \approx \pi \int_0^\infty dr r (\partial_r h_i)^2$ . Figure 5(a) shows the excess surface areas of the top and bottom, normalized by the initial value, as a function of dimensionless time  $\gamma t / (h_0 \eta)$  for three holes of different initial radii,  $r_0 = 2.3, 4.2,$  and  $6.2 \mu\text{m}$  on the same film. The trends are consistent with the intuition provided by Fig. 1(d), and the theoretical curves are in excellent agreement with the experimental data, which validates the hydrodynamic model. We further see that the top interface, which has an initially high excess surface area, exchanges energy with the bottom one, causing the excess surface area of the latter to initially increase. This happens through vertical flow, a process that continues until the top and bottom interfaces are mirror symmetric at  $\gamma t / (h_0 \eta) \sim 0.5$ , after which the excess surface areas of both interfaces are equal. At later times, the surface areas decrease as  $S \propto t^{-1/2}$  because of the self-similar

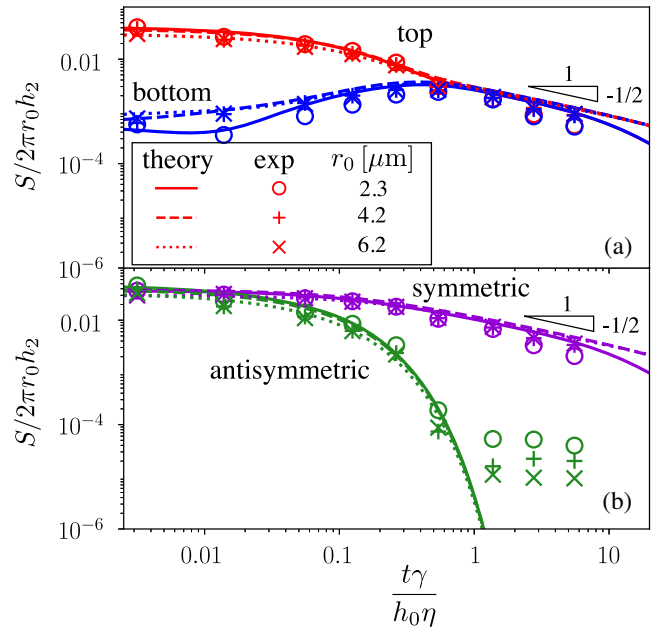


FIG. 5. Dimensionless excess surface area as a function of dimensionless time. The experimental data for three different holes are shown with different marker symbols, as indicated. The corresponding theoretical data are shown with different line styles, as indicated (fit parameter  $\gamma/\eta \approx 4.6 \times 10^{-5} \mu\text{m/s}$  [45]). (a) The top and bottom interfacial profiles. (b) The symmetric and antisymmetric modes. The slope triangles indicate power-law exponents.

properties of the heatlike equation that governs the symmetric mode.

One can define and plot the symmetric and antisymmetric surface areas  $S_{\text{sym}}$  and  $S_{\text{anti}}$  as functions of the dimensionless time [Fig. 5(b)]. The symmetric mode exhibits a long term  $S_{\text{sym}} \propto t^{-1/2}$  scaling, as a result of lateral flow. In contrast, the vertical flow in the antisymmetric mode dissipates energy more quickly, with a timescale  $\sim \eta h_0 / \gamma$  corresponding to the symmetrization time. The experiments reveal that this symmetrization time does not depend on the initial radius of the hole and is set by the dynamics of the slowest relaxation mode, i.e., the Fourier-Bessel mode  $k$  at which  $\lambda_{\text{anti}}(k)$  is minimal (Fig. 3) (the data at long times for the antisymmetric mode deviate from theory because of limitations in measuring a vanishing excess surface area).

We note that the governing equation of the antisymmetric mode is  $\frac{1}{6} \eta h_0^3 \partial_t \nabla^2 h_{\text{anti}} = \gamma h_{\text{anti}}$  in the long-wave limit. Upon taking the Laplacian of this expression, we recover on the right-hand side the Laplace pressure  $\delta P = \gamma \nabla^2 h_{\text{anti}}$  across the film. Then, the midplane line  $H = h_{\text{anti}}/2$  follows the equation  $\frac{1}{3} \eta h_0^3 \nabla^4 \partial_t H = \delta P$ . This equation corresponds to the torque balance in the liquid film [15,26,27] and is the viscous analog of the Föppl-von Kármán equation for an elastic membrane in pure bending, where the bending modulus is replaced by  $\eta h_0^3/3$

and the deflection field is replaced by the deflection rate  $\partial_t H$ .

In conclusion, we have reported on the symmetrization dynamics of cylindrical holes in freestanding polymer films. The topographies of both interfaces of the films were measured using AFM at various times, to track the evolution while they were annealed above the glass-transition temperature. The films were found to undergo a rapid symmetrization process in order to equilibrate the Laplace pressures of the two liquid-air interfaces. This process transfers excess surface energy between the two interfaces and eventually results in mirror-symmetric profiles on both sides of the film. A full-Stokes flow linear hydrodynamic model was developed and shown to be consistent with the observations. The model revealed the important roles of two modes, which differ by their symmetry with respect to the midplane of the film. The antisymmetric mode is associated with vertical flow, driven by the pressure gradient across the film, and exhibits faster dynamics than the symmetric mode, associated with lateral flow. The vertical symmetrization was found to occur on a universal timescale  $\eta h_0/\gamma$ , while the symmetric mode dominates at later times. Surprisingly, the evolutions of the interfacial profiles, when decomposed into the symmetric and antisymmetric components, are found to obey power laws, with the decrease in surface area of the symmetric mode scaling as  $t^{-1/2}$ , analogous to the heat equation.

We gratefully acknowledge financial support by the Natural Science and Engineering Research Council of Canada. We thank Hendrik Meyer for valuable discussions and Paul Fowler for help with preliminary experiments.

\*dalnoki@mcmaster.ca

†V. B. and J. N. contributed equally.

- [1] A. Oron, S. H. Davis, and S. G. Bankoff, *Rev. Mod. Phys.* **69**, 931 (1997).
- [2] R. V. Craster and O. K. Matar, *Rev. Mod. Phys.* **81**, 1131 (2009).
- [3] M. Tanaka and E. Sackmann, *Nature (London)* **437**, 656 (2005).
- [4] Y. Couder, J. Chomaz, and M. Rabaud, *Physica (Amsterdam)* **37D**, 384 (1989).
- [5] M. A. Rutgers, X. Wu, R. Bhagavatula, A. A. Petersen, and W. Goldburg, *Phys. Fluids* **8**, 2847 (1996).
- [6] A. Aradian, E. Raphaël, and P.-G. de Gennes, *Europhys. Lett.* **55**, 834 (2001).
- [7] D. Georgiev and P. Vorobieff, *Rev. Sci. Instrum.* **73**, 1177 (2002).
- [8] M.-J. Huang, C.-Y. Wen, I.-C. Lee, and C.-H. Tsai, *Phys. Fluids* **16**, 3975 (2004).
- [9] J. Seiwert, M. Monloubou, B. Dollet, and I. Cantat, *Phys. Rev. Lett.* **111**, 094501 (2013).
- [10] R. Stannarius, C. Bohley, and A. Eremin, *Phys. Rev. Lett.* **97**, 097802 (2006).
- [11] K. Harth, A. Eremin, and R. Stannarius, *Soft Matter* **7**, 2858 (2011).
- [12] A. Eremin, S. Baumgarten, K. Harth, R. Stannarius, Z. H. Nguyen, A. Goldfain, C. S. Park, J. E. MacLennan, M. A. Glaser, and N. A. Clark, *Phys. Rev. Lett.* **107**, 268301 (2011).
- [13] E. Villermaux, *Annu. Rev. Fluid Mech.* **39**, 419 (2007).
- [14] J. Nie, Z. Wang, Z. Ren, S. Li, X. Chen, and Z. L. Wang, *Nat. Commun.* **10**, 2264 (2019).
- [15] P. D. Howell, *Eur. J. Appl. Math.* **7**, 321 (1996).
- [16] N. M. Ribe, *J. Fluid Mech.* **457**, 255 (2002).
- [17] G. I. Taylor, in *Applied Mechanics* (Springer, New York, 1969), pp. 382–388.
- [18] G. Debrégeas, P.-G. de Gennes, and F. Brochard-Wyart, *Science* **279**, 1704 (1998).
- [19] R. da Silveira, S. Chaïeb, and L. Mahadevan, *Science* **287**, 1468 (2000).
- [20] A. Boudaoud and S. Chaïeb, *Phys. Rev. E* **64**, 050601(R) (2001).
- [21] N. M. Ribe, *Phys. Rev. E* **68**, 036305 (2003).
- [22] M. A. Biot, *Geol. Soc. Am. Bull.* **72**, 1595 (1961).
- [23] L. Guillou-Frottier, J. Buttles, and P. Olson, *Earth Planet. Sci. Lett.* **133**, 19 (1995).
- [24] J. R. Pearson, *Mechanics of Polymer Processing* (Springer, New York, 1985).
- [25] B. Scheid, S. Quiligotti, B. Tran, R. Gy, and H. A. Stone, *J. Fluid Mech.* **636**, 155 (2009).
- [26] G. Pfingstag, B. Audoly, and A. Boudaoud, *J. Fluid Mech.* **683**, 112 (2011).
- [27] S. Srinivasan, Z. Wei, and L. Mahadevan, *Phys. Rev. Fluids* **2**, 074103 (2017).
- [28] E. Ruckenstein and R. K. Jain, *J. Chem. Soc., Faraday Trans. 2* **70**, 132 (1974).
- [29] M. Prévost and D. Gallez, *J. Chem. Phys.* **84**, 4043 (1986).
- [30] T. Erneux and S. H. Davis, *Phys. Fluid A* **5**, 1117 (1993).
- [31] D. Vaynblat, J. R. Lister, and T. P. Witelski, *Phys. Fluids* **13**, 1130 (2001).
- [32] O. K. Matar, *Phys. Fluids* **14**, 4216 (2002).
- [33] S. S. Thete, C. Anthony, P. Doshi, M. T. Harris, and O. A. Basaran, *Phys. Fluids* **28**, 092101 (2016).
- [34] M. Ilton, C. DiMaria, and K. Dalnoki-Veress, *Phys. Rev. Lett.* **117**, 257801 (2016).
- [35] A. Choudhury, V. K. Paidi, S. K. Kalpathy, and H. N. Dixit, *arXiv:1902.11018*.
- [36] M. Ilton, M. M. P. Couchman, C. Gerbelot, M. Benzaquen, P. D. Fowler, H. A. Stone, E. Raphaël, K. Dalnoki-Veress, and T. Salez, *Phys. Rev. Lett.* **117**, 167801 (2016).
- [37] M. Backholm, M. Benzaquen, T. Salez, E. Raphaël, and K. Dalnoki-Veress, *Soft Matter* **10**, 2550 (2014).
- [38] G. Debrégeas, P. Martin, and F. Brochard-Wyart, *Phys. Rev. Lett.* **75**, 3886 (1995).
- [39] K. Dalnoki-Veress, B. G. Nickel, C. Roth, and J. R. Dutcher, *Phys. Rev. E* **59**, 2153 (1999).
- [40] C. B. Roth and J. R. Dutcher, *J. Polym. Sci. B* **44**, 3011 (2006).
- [41] J. D. McGraw, T. Salez, O. Bäümchen, E. Raphaël, and K. Dalnoki-Veress, *Soft Matter* **9**, 8297 (2013).
- [42] M. Benzaquen, T. Salez, and E. Raphaël, *Europhys. Lett.* **106**, 36003 (2014).

- [43] A. Bach, K. Almdal, H. K. Rasmussed, and O. Hassager, *Macromolecules* **36**, 5174 (2003).
- [44] J.D. Gaskill, *Linear Systems, Fourier Transforms, and Optics* (Wiley, New York, 1978), Vol. 576.
- [45] The fit value of  $\gamma/\eta \approx 4.6 \times 10^{-5} \mu\text{m/s}$  differs from experimental  $\gamma/\eta \approx 2.8 \times 10^{-4} \mu\text{m/s}$ . This is within experimental error given strong dependence of viscosities on temperature.